Journal of Magnetic Resonance 201 (2009) 7–17

Contents lists available at ScienceDirect

Journal of Magnetic Resonance

journal homepage: www.elsevier.com/locate/jmr

Heteronuclear decoupling by optimal tracking

Jorge L. Neves [a,1], Björn Heitmann [a,2], Navin Khaneja [b], Steffen J. Glaser [a,*]

[a] Department of Chemistry, Technische Universität München, 85747 Garching, Germany
[b] Division of Applied Sciences, Harvard University, Cambridge, MA 02138, USA

ARTICLE INFO

Article history:
Received 10 June 2009
Revised 19 July 2009
Available online 29 July 2009

Keywords:
Heteronuclear decoupling
Optimal control theory
GRAPE algorithm
Tracking
Average Hamiltonian theory

ABSTRACT

The problem to design efficient heteronuclear decoupling sequences is studied using optimal control methods. A generalized version of the gradient ascent engineering (GRAPE) algorithm is presented that makes it possible to design complex non-periodic decoupling sequences which are characterized by tens of thousands of pulse sequence parameters. In contrast to conventional approaches based on average Hamiltonian theory, the concept of optimal tracking is used: a pulse sequence is designed that steers the evolution of an ensemble of spin systems such that at a series of time points, a specified trajectory of the density operator is tracked as closely as possible. The approach is demonstrated for the case of low-power heteronuclear decoupling in the liquid state for *in vivo* applications. Compared to conventional sequences, significant gains in decoupling efficiency and robustness with respect to offset and inhomogeneity of the radio-frequency field were found in simulations and experiments.

1. Introduction

Heteronuclear decoupling methods have a long history in NMR spectroscopy [1–18]. The goal of broadband heteronuclear decoupling sequences is to collapse a spin I multiplet splitting by irradiating a spin S that is coupled to I in order to simplify the spectra and to increase the signal-to-noise ratio. At the same time, the decoupling sequence should introduce only a minimal amount of artifacts, such as decoupling sidebands. Furthermore, in order to avoid undesirable sample heating or damage to the probe, the radio frequency (rf) power of the decoupling sequence should be as small as possible. This is of particular importance in medical imaging or *in vivo* spectroscopy of humans. The earliest heteronuclear decoupling methods were based on cw irradiation [3] and noise decoupling [4]. Significantly improved decoupling sequences were found based on composite [1,2,5,7–9] or shaped [13–18] inversion pulses in combination with highly compensated cycles and supercycles [1,2,7,20–22]. Theoretical approaches that have been used for the analysis and design of decoupling sequences include average Hamiltonian [6,23] and Floquet [18] theory. Here we introduce a novel approach to decoupling where the decoupling pulse sequence is obtained by optimally tracking the evolution of a density matrix under a desired Hamiltonian. In particular we use this method to optimally track the evolution of a decoupled Hamiltonian. We show that the optimal control methods introduced in our previous work for transferring the state of the system closest to a desired target state can be generalized to make the evolution of the density matrix track a certain trajectory over an extended time period.

Recently, principles of optimal control theory [24] have found numerous applications in magnetic resonance. Theoretical limits for maximum heteronuclear transfer efficiency have been established for the typical NMR setting, where rf amplitudes can be much larger than heteronuclear couplings. Furthermore, in this limit of strong pulses, time-optimal [25,26] and relaxation-optimized [27,28] pulse sequences were derived, which achieve the theoretical limits. In addition to analytical bounds for the strong pulse limit, optimal-control based algorithms make it possible to numerically explore the physical limits of polarization transfer efficiency in realistic settings, where experimental limitations have to be taken into account. The GRAPE algorithm [29,30] has been successfully applied to problems in liquid-state NMR [31–38], solid-state NMR [39], and quantum information processing [40,41]. In the context of broadband heteronuclear decoupling, robust inversion pulses with minimal rf power [38] are potential candidates for inversion elements suitable for cyclic decoupling sequences. Alternatively, optimal control methods could be used to optimize decoupling elements that produce a desired effective Hamiltonian or an effective propagator over a small time period as demonstrated in [29,39,40]. However, both approaches do not use the full potential of optimal control methods.

Here, we introduce a more general method to design non-periodic, robust low-power decoupling sequences using tracking methods [24,42]. These methods fall into two categories. The first

* Corresponding author. Fax: +49 89 289 13210.
E-mail address: glaser@ch.tum.de (S.J. Glaser).
[1] Present address: Laboratório Nacional de Luz Síncrotron, Caixa Postal 6192, CEP 13083-970, Campinas-SP, Brazil.
[2] Present address: Bruker Biospin AG, 8117 Fällanden, Switzerland.

1090-7807/$ - see front matter © 2009 Elsevier Inc. All rights reserved.
doi:10.1016/j.jmr.2009.07.024

one attempts to exactly follow a desired output by some inversion method [43–47]. In the second approach, one tries to find an input control field that will approximate a desired output trajectory. These approximate methods can be constructive [48,49] or they can be based on the solution to an optimal control problem [50–54]. The application of the latter approach to heteronuclear decoupling sequences is presented in the following. The complexity resulting from considering non-periodic decoupling sequences can be handled with reasonable computational cost using efficient numerical methods. Potential applications range from NMR spectroscopy to quantum information processing. Here, we focus on the specific example of low-power decoupling sequences for *in vivo* applications, in order to illustrate the improved performance that can be achieved based on the presented optimal tracking approach.

2. Theory

We consider a system consisting of two heteronuclear spins 1/2 labeled I and S. We assume that spin I is observed while spin S is irradiated by a decoupling sequence. In a doubly rotating frame, the Hamiltonian has the form

$$\mathscr{H}(t) = \mathscr{H}^I_{off} + \mathscr{H}^S_{off} + \mathscr{H}^{IS}_J + \mathscr{H}^S_{rf}(t), \tag{1}$$

with the offset term of spin I

$$\mathscr{H}^I_{off} = 2\pi\nu_I I_z, \tag{2}$$

the offset term of spin S

$$\mathscr{H}^S_{off} = 2\pi\nu_S S_z, \tag{3}$$

the heteronuclear J coupling term

$$\mathscr{H}^{IS}_J = 2\pi J S_z I_z, \tag{4}$$

and the rf term representing the decoupling sequence

$$\mathscr{H}^S_{rf}(t) = 2\pi\epsilon\{u_x(t)S_x + u_y(t)S_y\}. \tag{5}$$

The controls $u_x(t)$ and $u_y(t)$ are the nominal amplitudes of the x and y components of the rf field in the doubly rotating frame and ϵ is a rf scaling factor, which takes into account rf inhomogeneity and miscalibration effects. As $\mathscr{H}^I_{off}$ commutes with the terms $\mathscr{H}^S_{off}$, $\mathscr{H}^{IS}_J$, and $\mathscr{H}^S_{rf}(t)$, the offset effect of spin I can be separated and it is sufficient to consider the simplified Hamiltonian

$$\mathscr{H}'(t) = \mathscr{H}^S_{off} + \mathscr{H}^{IS}_J + \mathscr{H}^S_{rf}(t), \tag{6}$$

for the analysis and design of heteronuclear decoupling sequences, i.e. spin I can be assumed to be on resonance. We assume the initial density operator to be

$$\rho(t_0) = I_x. \tag{7}$$

In the absence of a decoupling sequence, $\mathscr{H}^S_{rf}(t) = 0$, the offset term $\mathscr{H}^S_{off}$ commutes both with $\rho(t_0)$ and with $\mathscr{H}^{IS}_J$ and hence the evolution of the density operator is simply governed by the coupling term $\mathscr{H}^{IS}_J$:

$$\rho(t) = I_x\cos(\pi Jt) + 2I_yS_z\sin(\pi Jt), \tag{8}$$

and the cosine modulation of the detectable operator I_x results in a doublet with splitting J in the resulting spectrum after Fourier transformation of the time-domain signal corresponding to the expectation value $\langle I_x\rangle(t)$. In typical experimental settings, the signal is not detected continuously, but only at a number of discrete time points T_k. As illustrated in Fig. 1, the digitization of the decoupling sequence (with time slices $\Delta t = t_{m+1} - t_m$) is typically finer than the digitization of the detected signal (with time intervals $\Delta T = T_{k+1} - T_k$) and $M = \Delta T/\Delta t$ is the number of time slices Δt per interval ΔT. Hence, if the signal is detected at the $N+1$ time points $T_0,\ldots,T_N$, the entire decoupling sequence consists of NM time slices and is characterized by NM control amplitudes $u_x(j)$ and by NM control amplitudes $u_y(j)$ with $1 \leqslant j \leqslant NM$. In the case of perfect decoupling, the desired evolution of the density operator is

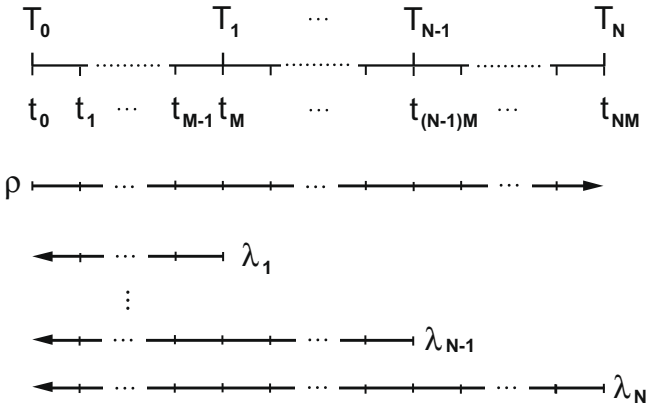

Fig. 1. Schematic representation of the acquisition points T_k (with $0 \leqslant k \leqslant N$) and the digitization of a heteronuclear decoupling sequence, consisting of M time slices $\Delta t = t_{m+1} - t_m$ between two subsequent acquisition points. Rf amplitudes are optimized for a total of N times M time slices. The density operator $\rho(0) = I_x$ evolves forward in time and for each acquisition point, there is a costates $\lambda_k(T_k) = I_x$ that is evolved backward in time. As shown in Appendix 3, the backward evolution of the N costates λ_k can be reduced to a single backward evolution of the combined costate Λ.

$$\rho_d(T_k) = I_x \quad \text{for } 0 \leqslant k \leqslant N, \tag{9}$$

i.e. the expectation value $\langle I_x\rangle(t)$ of the detection operator is constant at all time points T_k where a signal is detected. In this case, no splitting is observed in the resulting spectrum after Fourier transformation. Here, we demonstrate how to design heteronuclear decoupling sequences by tracking this desired evolution of the density operator at specified time points T_k, where the signal is detected during the free induction decay. The optimal tracking problem can be efficiently solved using an extended version of the GRAPE algorithm [29]. In the original version of GRAPE, the quality factor for state to state transfer is defined as the projection of the final density operator $\rho(T)$ onto a desired target operator C. The gradient of this quality factor with respect to the control amplitudes (i.e. the pulse sequence parameters) can be calculated efficiently from the density operator $\rho(t)$ that evolves forward in time starting from $\rho(0)$ and a so-called costate operator $\lambda(t)$ that evolves backward in time starting from $\lambda(T) = C$. In the case of heteronuclear decoupling, the projection of the density operator on a series of desired target operators $C(T_k) = I_x$ is relevant for all time points T_k at which the signal is detected. As shown in the following, in this case the gradient of the corresponding quality factor for decoupling can be calculated efficiently from the density operator $\rho(t)$ and a series of costate operators $\lambda_k(t)$ that evolve backward in time starting from $\lambda_k(T_k) = C(T_k) = I_x$ (c.f. Fig. 1).

The quality of decoupling can be quantified by the signal amplitude of the decoupled resonance line in the frequency domain. In addition, the amplitude of decoupling sidebands should be as small as possible. As according to the simplified Hamiltonian $\mathscr{H}'(t)$ (c.f. Eq. (6)) spin I can be assumed to be on-resonance, the amplitude of the spin I spectrum at zero frequency is simply given by the Fourier transform of the free induction decay at frequency $\nu_I = 0$. The detected discrete time-domain signal is

$$s_k = \langle I_x\rangle(T_k) = \mathrm{Tr}\{I_x\rho(T_k)\}, \tag{10}$$

i.e. the expectation value of I_x at the time points T_k. As I_x is Hermitian, i.e. $I_x = I_x^\dagger$, Eq. (10) can also be written in the form

$$s_k = \mathrm{Tr}\{I_x^\dagger \rho(T_k)\} = \langle I_x \mid \rho(T_k)\rangle, \tag{11}$$

i.e. as the projection of the density operator $\rho(T_k)$ onto the detection operator I_x [29,55]. For the typical case of linear sampling, the time points T_k are evenly spaced over the acquisition time T_{acq} and the dwell time $\Delta T = T_{k+1} - T_k$ is given by T_{acq}/N, where $N+1$ is the number of detected time points. (In the case of nonlinear sampling, the time points T_k can be chosen according to the desired sampling scheme.) The discrete Fourier transform S_l of the time-domain signal amplitudes s_k has the form [55]

$$S_l = \frac{1}{N+1}\sum_{k=0}^{N} s_k \exp\{-i2\pi kl/(N+1)\}. \tag{12}$$

Hence the relevant quality factor representing the amplitude of a decoupled on-resonance signal in the spin I spectrum for a given rf scaling factor ϵ (c.f. Eq. (5)) and offset ν_S is given by Eq. (12) for $l = 0$:

$$\begin{aligned}\phi(\epsilon,\nu_S) = S_0(\epsilon,\nu_S) &= \frac{1}{N+1}\sum_{k=0}^{N} s_k(\epsilon,\nu_S)\\ &= \frac{1}{N+1}\sum_{k=0}^{N}\langle I_x \mid \rho(\epsilon,\nu_S,T_k)\rangle.\end{aligned} \tag{13}$$

The overall performance function Φ for a decoupling sequence can be defined as the quality factors $\phi(\epsilon,\nu_S)$ averaged over all offsets ν_S and rf scaling factors ϵ of interest. For simplicity, here we assume an equal weight for all offsets and scaling factors, resulting in the overall performance function

$$\Phi = \frac{1}{N_\epsilon N_\nu}\sum_{p=1}^{N_\epsilon}\sum_{q=1}^{N_\nu}\phi\left(\epsilon^{(p)},\nu_S^{(q)}\right), \tag{14}$$

with N_ϵ discrete rf scaling factors $\epsilon^{(p)}$ and N_ν discrete offsets $\nu_S^{(q)}$ that are evenly spaced in the desired range of rf scaling factors and offset frequencies for a given application.

In principle, the gradient $\delta\Phi/\delta u_\alpha(j)$ (for $\alpha = x$ and y) of the overall performance function Φ with respect to the $2NM$ control amplitudes $u_\alpha(j)$ could be calculated using the difference method, in which $\delta\Phi/\delta u_\alpha(j)$ is approximated by $\Delta\Phi/\Delta u_\alpha(j)$, where $\Delta\Phi = \Phi(u_\alpha(j) + \Delta u_\alpha(j)) - \Phi(u_\alpha(j))$. However, with the help of optimal control methods the same gradient can be calculated orders of magnitude faster by using the known equation of motion for the density operator. This makes it possible to optimize entire non-cyclic decoupling sequences with a very large number of pulse sequence parameters (i.e. control amplitudes $u_\alpha(j)$) from scratch.

Following the approach described in [29], general analytical expressions for the gradient $\delta\Phi/\delta u_\alpha(j)$ to first order in Δt are derived in Appendix 1 for the case of an arbitrary relaxation matrix. If the relevant terms of the density operator relax with similar rates, simplified expressions for $\delta\Phi/\delta u_\alpha(j)$ can be derived, as shown in Appendix 2. This simple case is assumed in the following in order to demonstrate the tracking approach for heteronuclear decoupling. Here we focus on the case where the dynamics of the density operator $\rho(t)$ under the Hamiltonian $\mathscr{H}'(t)$ (c.f. Eq. (6)) is restricted to the subspace spanned by the operators I_x, $2I_yS_x$, $2I_yS_y$, $2I_yS_z$ and where these terms all decay with the same relaxation rate κ. As shown in Appendix 2, in this case the general form of the gradient for the quality factor $\phi(\epsilon,\nu_S)$ (c.f. Eq. (13)) with respect to the control amplitudes $u_x(j)$ and $u_y(j)$ of all time slices ($1 < j \leqslant MN$) as derived in Appendix 1 simplifies to

$$\begin{aligned}\frac{\delta\phi(\epsilon,\nu_S)}{\delta u_\alpha(j)} &= \frac{1}{N+1}\sum_{k>l}\frac{\delta s_k}{\delta u_\alpha(j)}\\ &= \mathrm{i}\ 2\pi\epsilon\Delta t\ \frac{1}{N+1}\\ &\quad\times\sum_{k>l}\exp\{-\kappa\ T_k\}\ \langle S_\alpha|[\rho'(t_j),\lambda'_k(t_j)]\rangle\\ &= \mathrm{i}\ 2\pi\epsilon\Delta t\ \frac{1}{N+1}\langle S_\alpha|[\rho'(t_j),\Lambda(t_j)]\rangle,\end{aligned} \tag{15}$$

where $\alpha = x$ or y. Here

$$\rho'(t_j) = U_j\ldots U_1\ \rho(t_0)\ U_1^\dagger\ldots U_j^\dagger, \tag{16}$$

is the density operator at time point t_j that is obtained by unitarily evolving the initial density operator $\rho(0) = I_x$ forward in time. We call

$$\lambda'_k(t_j) = U_{j+1}^\dagger\ldots U_{kM}^\dagger\ C(T_k)\ U_{kM}\ldots U_{j+1}, \tag{17}$$

the kth costate at time point t_j that is obtained by unitarily evolving the target or detection operator $C(T_k) = I_x$ backward in time (c.f. Appendix 2). In this simplified model, all relaxation effects are contained in the damping term $\exp\{-\kappa\ T_k\}$. The integer $l = \lfloor j/M\rfloor$ is the truncated value (also called floor function or integral value) of the ratio j/M, i.e. the number of complete intervals ΔT before the jth time slice. The condition $k > l$ for the summation in Eq. (15) reflects the fact that the control amplitudes $u_x(j)$ and $u_y(j)$ in the jth time slice cannot affect the detected signal at earlier detection points. The operator $\Lambda(t_j)$ in Eq. (15) is defined as

$$\Lambda(t_j) = \sum_{k>l}\exp\{-\kappa\ T_k\}\ \lambda'_k(t_j), \tag{18}$$

and can efficiently be calculated for all time points $t_0 \leqslant t_j \leqslant T_N$ as detailed in Appendix 3.

In the case discussed here, where under the action of $\mathscr{H}'(t)$ (c.f. Eq. (6)) the relevant dynamics of the density operator $\rho(t_j)$ and the costate operators $\lambda_k(t_j)$ is restricted to the subspace spanned by basis operators $2I_yS_x$, $2I_yS_y$, $2I_yS_z$, and S_x, the calculation of unitary evolution in this subspace can further be significantly accelerated by introducing reduced four-dimensional state vectors (c.f. Appendix 4) [56–58]. In analogy to the three-dimensional Bloch vector representation of the density operator for a single uncoupled spin, the expectation values of the terms $2I_yS_x$, $2I_yS_y$, $2I_yS_z$, and I_x, form the elements of a four-dimensional vector that captures the dynamics of the density operator that is relevant for the simulation and optimization of heteronuclear decoupling sequences. In Appendix 4, the reduced state and costate vectors $\vec{\rho}$ and $\vec{\lambda}_k$ as well as $\vec{\Lambda}$ are defined and an explicit form of the corresponding reduced propagator $\mathbf{U}(j)$ [56–58] for each time slice j is given in the Supplementary material.

Finally, the gradient for the overall quality function Φ (c.f. Eq. (14)) is given by the averaged gradients $\delta\phi(\epsilon,\nu_S)/\delta u_\alpha(j)$:

$$\frac{\delta\Phi}{\delta u_\alpha(j)} = \frac{1}{N_\epsilon N_\nu}\sum_{p=1}^{N_\epsilon}\sum_{q=1}^{N_\nu}\frac{\delta\phi\left(\epsilon^{(p)},\nu_S^{(q)}\right)}{\delta u_\alpha(j)}. \tag{19}$$

The performance function Φ can be increased by following this gradient, i.e. if we choose

$$u_\alpha(j)\ \rightarrow\ u_\alpha(j)\ +\ \varepsilon\ \frac{\delta\Phi}{\delta u_\alpha(j)}, \tag{20}$$

where ε is a small step size. This forms the basis of the following generalized version of the GRAPE algorithm [29] for optimal tracking of a desired evolution of the density operator, which can be readily applied to the problem of efficient and robust low-power heteronuclear decoupling.

For the case of uniform relaxation rates κ considered here, the basic GRAPE tracking algorithm based on the reduced four-dimensional state and costate vectors (c.f. Appendix 4) can be summarized as follows:

(1) Guess initial controls $u_x(j)$ and $u_y(j)$ for $1 \leqslant j \leqslant NM$.
(2) Starting from $\vec{\rho}(0) = (0,0,0,1)^T$, calculate $\vec{\rho}'(t_j)$ for $1 \leqslant j \leqslant NM$ using Eq. (45).
(3) Starting from $\vec{\Lambda}(T_N) = \exp\{-\kappa\, T_N\}(0,0,0,1)^T$, calculate $\vec{\Lambda}(t_j)$ for $1 \leqslant j \leqslant NM$ using Eq. (52).
(4) Calculate $\delta\phi(\epsilon^{(p)}, \nu_S^{(q)})/\delta u_\alpha(j)$ for $1 \leqslant j \leqslant NM$ using Eqs. (50) and (51).
(5) Repeat steps 2–4 for all scaling factors $\epsilon^{(p)}$ and offsets $\nu_S^{(q)}$ and calculate $\delta\Phi/\delta u_x(j)$ and $\delta\Phi/\delta u_y(j)$ using Eq. (19).
(6) Update the $2NM$ control amplitudes $u_x(t_j)$ and $u_y(t_j)$ according to Eq. (20).
(7) With these as the new controls, go to step 2.

The algorithm is terminated if the change in the performance index Φ is smaller than a chosen threshold value. In practice, the gradient information (Eq. (19)) can be used in more general optimizing algorithms for faster convergence, such as conjugate gradient or quasi-Newton methods. For general relaxation superoperators, the algorithm can be modified using the general form of the gradient $\delta\Phi/\delta u_\alpha(j)$ given in Appendix 1. The rf power of the decoupling sequence can be minimized or fixed as described in [29,38]. The maximum rf amplitude u_{max} can be limited by resetting the amplitude to the maximum amplitude if it is exceeded after step 6 [29,31]. If a constant rf amplitude u_0 is desired [35], the update rule of Eq. (20) for the rf amplitudes $u_x(j)$ and $u_y(j)$ can be replaced by the corresponding update rule for the rf phases $\varphi(j)$:

$$\varphi(j) \;\rightarrow\; \varphi(j) \;+\; \varepsilon\, \frac{\delta\Phi}{\delta\varphi(j)}, \tag{21}$$

with

$$\frac{\delta\Phi}{\delta\varphi(j)} = u_0\left\{-\frac{\delta\Phi}{\delta u_x(j)}\sin\varphi(j) + \frac{\delta\Phi}{\delta u_y(j)}\cos\varphi(j)\right\}. \tag{22}$$

3. Pulse sequence optimizations

In order to demonstrate the spin-tracking approach for the development of efficient heteronuclear decoupling sequences and to compare their performance with state-of-the-art experiments, we focus on experimental settings typical for *in vivo* applications [19]. Maximum suitable rf amplitudes for human applications are on the order of 500 Hz at 4 T.

In this low power case, the best known sequences are MLEV-16 [5] (with a decoupling bandwidth of ±435 Hz) and WALTZ-16 [7] (with a decoupling bandwidth of ±410 Hz), which outperform other known decoupling sequences, including sequences based on adiabatic pulses [19]. In our study, we set the desired decoupling bandwidth to 1 kHz, i.e. $-500\text{ Hz} \leqslant \nu_S \leqslant 500\text{ Hz}$. This offset range was digitized in steps of 50 Hz, resulting in $N_\nu = 21$ offset points. As in [19], we assumed a linewidth of 6 Hz, corresponding to a transverse relaxation time of $T_2 = 1/(\pi 6\text{ Hz}) = 53$ ms and a corresponding relaxation rate $\kappa = 1/T_2 = 18.8\text{ s}^{-1}$. For the optimizations, we assumed a heteronuclear coupling constant of $J = 140$ Hz which represents an approximate value for sp^3 hybridized CH_n groups that was also used in the recent comparative study of various decoupling sequences [19]. We assumed a dwell time ΔT of 1 ms (corresponding to a spectral range of 1 kHz for spin I) and $N = 128$ time steps ΔT, resulting in a total acquisition time of 128 ms. Each interval ΔT between two detection points was partitioned into $M = 40$ time slices with $\Delta t = 25$ μs. Hence, a complete non-periodic decoupling sequence consists of $NM = 5120$ time slices, i.e. there is a total of 10,240 control parameters $u_x(j)$ and $u_y(j)$ with $1 \leqslant j \leqslant NM = 5120$ to be optimized. Here, we limited the maximum rf amplitude and the optimizations resulted in decoupling sequences in which during virtually all time slices Δt the maximum allowed nominal rf amplitude u_{max} was reached. We therefore reoptimized the resulting sequences enforcing a constant nominal rf amplitude $u_0 = u_{max}$. This resulted in purely phase-modulated decoupling sequences, which can be implemented experimentally more conveniently and e.g. do not require linear amplifiers. Optimizations starting with different random initial pulse sequences resulted in different decoupling sequences but with similar performance. Typical durations of the optimization of a tracking-based decoupling sequence were on the order of 16 hours on a PC.

To explore the achievable quality of decoupling as a function of the nominal rf amplitude u_0 (assuming $\epsilon = 1$), we optimized a series of ten tracking-based decoupling sequences for $0\text{ Hz} < u_0 \leqslant 500$ Hz (c.f. solid circles in Fig. 2A and B). Reasonable decoupling efficiency ($\Phi > 0.9$) is found if u_0 is on the order of 360 Hz or larger. We also optimized shorter basis sequences of duration 64 ms (open circles), 32 ms (solid square), 16 ms (open squares), 8 ms (solid diamonds), 4 ms (open diamonds), 2 ms (solid

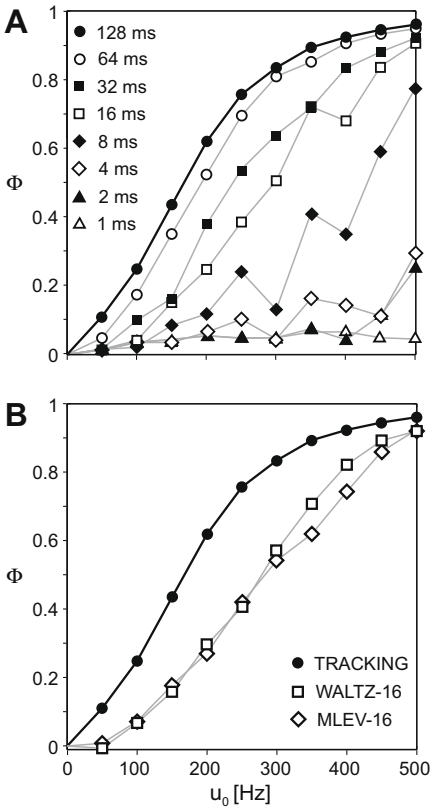

Fig. 2. For the offset range of $500\text{ Hz} \leqslant \nu_S \leqslant 500$ Hz and no rf scaling ($\epsilon = 1$), the decoupling quality Φ (normalized relative to the perfectly decoupled peak amplitudes) is shown as a function of the nominal rf amplitude u_0 for various decoupling schemes. In (A) and (B), the solid circles represent quality factors of tracking-based, non-periodic decoupling sequences optimized for the total acquisition time T_{acq} consisting of $N = 128$ periods $\Delta T = 1$ ms. (A) Also shows quality factors of periodic decoupling sequences, which consist of tracking-based basis sequences with durations of 64 ms (open circles), 32 ms (solid square), 16 ms (open squares), 8 ms (solid diamonds), 4 ms (open diamonds), 2 ms (solid trinagles) and 1 ms (open triangles). For comparison, the performance of MLEV-16 (open diamonds) [5] and WALTZ-16 (open squares) [7] is shown in (B) as a function of the nominal rf amplitude u_0.

triangles) and 1 ms (open triangles) and Fig. 2A shows the resulting decoupling quality if these shorter basis sequences are repeated periodically during the entire acquisition time of 128 ms. While the decoupling efficiency for a single application of these numerically optimized basis sequences of short durations is monotonically and smoothly increasing for increasing nominal rf amplitude (data not shown), the erratic variations of the decoupling efficiency as a function of u_0 in Fig. 2A reflect the fact that small error terms may or may not accumulate coherently if these basis sequences are simply periodically repeated. The simulations show increasing decoupling efficiency with increasing duration of the basis sequence and the best tracking-based decoupling efficiency is achieved by the non-periodic decoupling sequences (solid circles). For comparison, the performance of the MLEV-16 (open diamonds) [5] and WALTZ-16 (open squares) [7] sequences is shown in Fig. 2B as a function of the nominal rf amplitude u_0. These decoupling sequences consist of periodically repeated supercycles of duration $16/u_0$ and $24/u_0$ for MLEV-16 and WALTZ-16, respectively. For example, for a nominal rf amplitude $u_0 = 200$ Hz, the duration of the WALTZ-16 supercycle is 120 ms (corresponding almost to the entire duration of the detection period), whereas for $u_0 = 500$ Hz the duration of the WALTZ-16 cycle is 48 ms.

After these initial studies, where for simplicity an ideal rf scaling factor of $\epsilon = 1$ was assumed, we proceeded to optimize tracking-based decoupling sequences that are robust with respect to rf inhomogeneity, which can be substantial for *in vivo* applications depending on rf coil geometry. As rf amplitudes of less than 500 Hz are desirable, we chose a challenging test case corresponding to a nominal rf amplitude u_0 of only 400 Hz and an rf scaling factor ϵ between 0.7 and 1.0, resulting in actual rf amplitudes $v_{rf} = \epsilon u_0$ in the range 280 Hz $\leqslant v_{rf} \leqslant$ 400 Hz. The rf scaling factor ϵ was digitized in steps of 0.03, resulting in $N_\epsilon = 11$ discrete values (c.f. Eq. (5)). For a comparison of different experimental settings, it is convenient to express not only the rf scaling factor $\epsilon = v_{rf}/u_0$ but all relevant frequency parameters for the optimization problem relative to u_0 (or relative to $u_{rms} = \left\{\sum_{j=1}^{NM}\left(u_x^2(j) + u_y^2(j)\right)/NM\right\}^{1/2}$ for decoupling sequences with variable rf amplitudes if the rf power is limited). In terms of these unitless parameters, the chosen optimization problem corresponds to a relative decoupling bandwidth of $\Delta\nu_S/u_0 = 1000$ Hz/400 Hz $= 2.5$, a relative heteronuclear J coupling $J/u_0 = 140$ Hz/400 Hz $= 0.35$, a relative sampling frequency $(\Delta T)^{-1}/u_0 = (1\text{ ms})^{-1}/400\text{ Hz} = 2.5$, a relative acquisition time $T_{acq}/u_0^{-1} = 128\text{ ms}/2.5\text{ ms} = 51.2$ and rf scaling factors $\epsilon = v_{rf}/u_0$ in the range $0.7 \leqslant \epsilon \leqslant 1$.

Fig. 3A shows the phase modulation $\phi(t)$ of a resulting tracking-based, non-periodic decoupling sequence which we will refer to as TRACK-1 in the following and which is available in electronic form in the Supplementary material and at http://www.org.chemie.tu-muenchen.de/glaser/Downloads.html. For comparison, the periodic phase modulation of the MLEV-16 decoupling sequence with the same nominal rf amplitude of $u_0 = 400$ Hz (and a corresponding duration of a MLEV-16 supercycle of $16/u_0 = 40$ ms) is shown in Fig. 3B. In Fig. 4, examples of simulated FIDs (without damping) and the corresponding Fourier transformed spectra (after a damping of the FID corresponding to a linewidth of 6 Hz) are shown for offsets $\nu_S = -500$, 0, and 500 Hz for TRACK-1, MLEV-16 [5] and WALTZ-16 [7]. For all offsets, the undamped FID of the TRACK-1 sequence shows the largest amplitude and the least modulations and consequently yields the largest decoupled signal and the smallest sideband amplitudes compared to conventional decoupling sequences. Scaled figures with additional offsets are shown in the Supplementary material to make the detailed structure of the sidebands more visible. A more comprehensive view of the theoretical and experimental decoupling quality as a function of relative offset ν_S/u_0 and rf scaling ϵ is given in Figs. 5 and 6 for TRACK-1, MLEV-16 and WALTZ-16. In these figures, the range $-1.25 \leqslant \nu_S/u_0 \leqslant 1.25$ and $0.7 \leqslant \epsilon \leqslant 1$ for which the TRACK-1 decoupling sequence was optimized is indicated by a dashed rectangle. Fig. 5 shows simulated and experimental signal amplitudes S_0 corresponding to the quality factor $\phi(\epsilon, \nu_S)$ (c.f. Eq. (13)) and Fig. 6 shows the amplitude of the largest decoupling sidebands. Although the TRACK-1 sequence was specifically optimized for a dwell time ΔT of 1 ms (corresponding to a spectral width of $1/\Delta T$ of 1 kHz), the sequence also works well for shorter dwell times (and correspondingly larger spectral widths). This is expected as the rf amplitude and offset range of spin S limit potential modulations of the decoupled FID (and of corresponding decoupling sidebands) to be on the order of about 500 Hz or less. In the experiments for Figs. 5 and 6, the $I-S$ spin system was represented by the ^{1}H–^{13}C moiety of ^{13}C sodium formate dissolved in D_2O. In this molecule, the heteronuclear ^{1}H–^{13}C coupling constant $J' = 195$ Hz is a factor of 1.39 larger than the coupling constant $J = 140$ Hz (typical for sp^3 hybridized CH_n groups) that was used in the optimizations and simulations. In order to make the experimental results directly comparable to the simulations, we scaled the experimental parameters such as to have the same relative values of J'/u_0', $(\Delta T')^{-1}/u_0'$, and $T_{acq}'/u_0'^{-1}$, resulting in $u_0' = 557$ Hz, and $\Delta T' = 0.71$ ms. The experimental signal amplitudes are normalized relative to a reference experiment using on-resonance MLEV-16 decoupling with an rf amplitude of 2 kHz. The experiments were performed on a Bruker AC 200 spectrometer operating at a Larmor frequency of 200 MHz for ^{1}H and 50 MHz for ^{13}C. The residual water (HDO) signal was suppressed by presaturation and no digital filtering was used in the experiments. Both in the simulations and in the experiments, TRACK-1, MLEV-16, and WALTZ-16 decoupling sequences were applied in synchronized mode, i.e. each decoupling sequence was started at the beginning of the acquisition period. Zero filling to 64 k was used prior to Fourier transformation. For each decoupling sequence, experimental spectra were acquired for 27 rf scaling factors in the range between 0 and 1.625 u_0 by changing the attenuation setting of the ^{13}C decoupling channel without changing the timing of the sequences. For each scaling factor, 23 experiments were performed for offsets ν_S' in the range between $-1.375\,u_0$

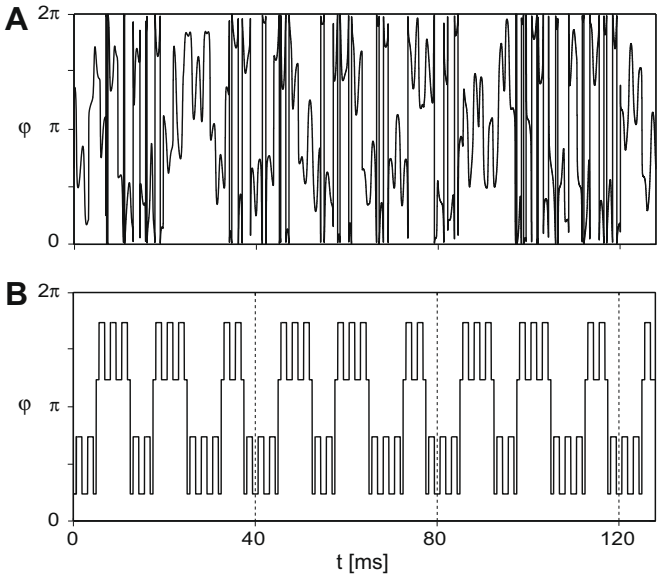

Fig. 3. Phase modulation $\phi(t)$ of the non-periodic TRACK-1 heteronuclear decoupling sequence for a total acquisition time T_{acq} of 128 ms (A) and of the periodic MLEV-16 sequence [5] (B) with a nominal rf amplitude $u_0 = 400$ Hz. The individual, periodically applied MLEV-16 supercycles (with a duration of $16/u_0 = 40$ ms) are indicated by dashed vertical lines.

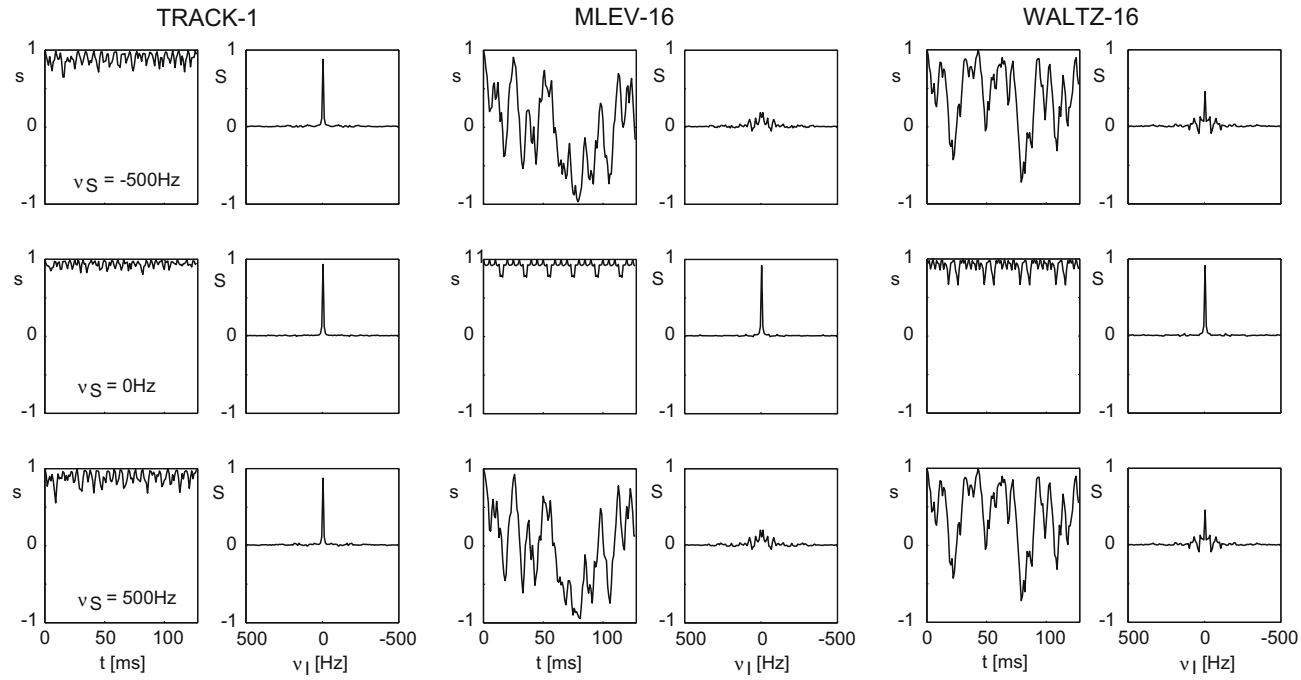

Fig. 4. For TRACK-1, MLEV-16 and WALTZ-16 with a nominal rf amplitude $u_0 = 400$ Hz and $\epsilon = 1$, simulated FIDs without damping (left column) and the corresponding spectra (normalized relative to the perfectly decoupled peak amplitude) with a damping of the FID before Fourier transformation corresponding to a linewidth of 6 Hz (right column) are shown for offsets $\nu_S = -500$ Hz (top row), 0 Hz (middle row), and 500 Hz (bottom row).

and 1.375 u_0. Hence each subplot in Figs. 5 and 6 represent a total of 621 experiments. A reasonable match is found between simulations and experiments. Remaining differences can be attributed to experimental imperfection, such as rf inhomogeneity of about ±5%. In the target range of offset and rf scaling, the TRACK-1 sequence performs markedly better than all known conventional sequences, both in terms of signal amplitude and sideband intensity. As expected [19], MLEV-16 performs slightly better than WALTZ-16 under these conditions. For TRACK-1 and MLEV-16, cross sections (for $\epsilon = 0.87$, 0.79, and 0.71) of the plots of Fig. 5 are shown in Fig. 7 to provide a better comparison of the decoupled signal amplitudes. In the simulations as well as in the experimental spectra, the TRACK-1 decoupling sequence resulted in larger signal amplitudes and in a significant increase of the decoupling bandwidth by more than 50%.

We also applied the TRACK-1 sequence for ^{13}C-decoupling in an HSQC experiment of α/β-D-glucose dissolved in D_2O at a ^{1}H frequency of 200 MHz. The resulting two-dimensional spectrum is shown in Fig. 8A. Fig. 8B shows the corresponding spectrum for MLEV-16 decoupling. In this sample, the heteronuclear ^{1}H–^{13}C coupling constants are approximately 140 Hz, corresponding to the value used in the optimization. In both experiments, a nominal rf amplitude for decoupling of 400 Hz was used, corresponding to a duration of 1.25 ms for an inversion pulse. The ^{13}C resonances of C_2, C_3, C_4, C_5, and C_6 are in the spectral range between 59 and 79 ppm. This frequency range corresponds to the optimized decoupling bandwidth of 1 kHz and the ^{13}C transmitter frequency was set to the center of this chemical shift range at 69 ppm. Four distinct groups of cross peaks for the two anomers are found (cross peaks of C_3 and C_5 are overlapping). The gains of the corresponding integrated cross peak amplitudes for TRACK-1 versus MLEV-16 decoupling were 2% (C_4), 9.5% (C_2), 16% (C_3/C_5), and 25% (C_6). As expected from the simulated and experimental data shown in Fig. 5, the largest gains are found for the C_3/C_5 and C_6 cross peaks (see cross sections in Fig. 8C), which have the largest offsets relative to the ^{13}C transmitter frequency.

4. Discussion and conclusion

The most important criterion for efficient decoupling is the amplitude of the decoupled signals. The presented spin-tracking approach is a natural and direct consequence of this criterion. The efficient calculation of high-dimensional gradients for tens of thousands of pulse sequence parameters makes is possible to optimize non-periodic decoupling sequences for the entire duration of the acquisition time. Although the phase modulation of the TRACK-1 sequence appears to be stochastic (c.f. Fig. 3A), it is important to note that this is not the case. In contrast to the technique of pseudo-random phase modulation, or noise decoupling [4], tracking-based decoupling sequences such as TRACK-1 are deterministic sequences with well defined trajectories of the spins for the desired range of offsets and rf scaling factors during the entire duration of the detection period. As demonstrated both by simulations and experiments, this can provide significantly better performance than previously known decoupling sequences. In the tracking approach, imperfections that cannot be compensated for on a short time scale do not accumulate but can be corrected on a longer time scale, taking into account the characteristic relaxation rates of the spin system. The presented tracking approach takes into account the fact that the rf amplitudes during a given time slice of the decoupling sequence affect the trajectory of the density operator and hence the detected signal not only for the next, but for all following time points. Conversely, in the optimization algorithm, the signal amplitudes of all following detection points have an influence on the rf parameters of each time slice, weighted by relaxation effects. (This is in contrast to algorithms that take only into account the next detection point [59], which is in general not optimal, because the sequence that leads to the best result at T_{k+1} is not necessarily the beginning of the one giving best results at T_{k+2} etc.) The number of following detection points that are taken into account is large for time slices near the beginning and small near the end of the acquisition time. This kind of asymmetry is not taken into account in periodic decoupling sequences and in conven-

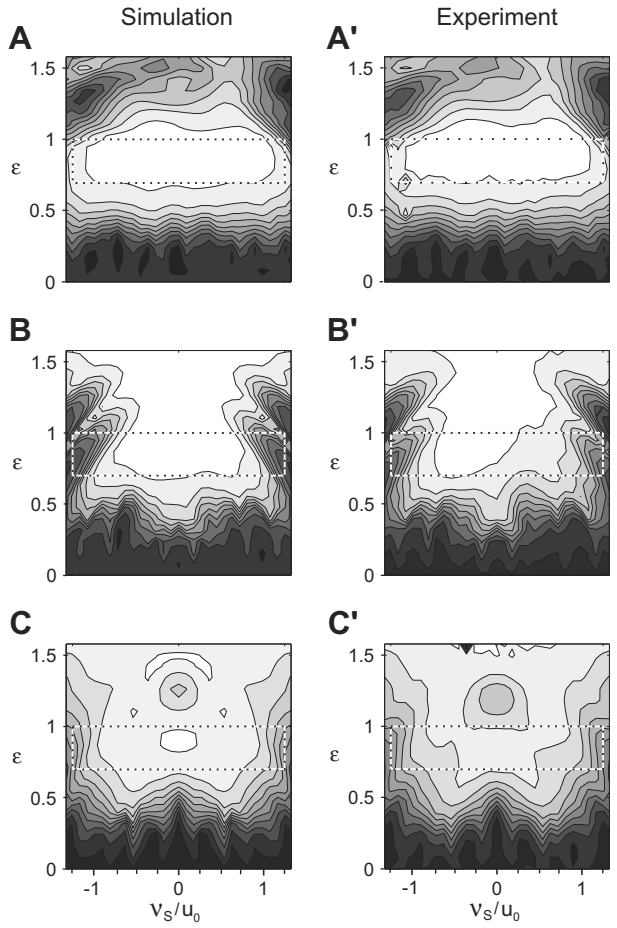

Fig. 5. Simulated (left column) and experimental (right column) signal amplitudes S_0 (normalized relative to the perfectly decoupled peak amplitude), corresponding to quality factors $\phi(\epsilon, \nu_S)$, are shown as a function of relative offset ν_S/u_0 and rf scaling ϵ for (A,A′) TRACK-1, (B,B′) MLEV-16 and (C,C′) WALTZ-16. Contour levels are shown in steps of 0.1, white areas corresponds to $S_0 > 0.9$. The range $-1.25 \leqslant \nu_S/u_0 \leqslant 1.25$ and $0.7 \leqslant \epsilon \leqslant 1$ for which the TRACK-1 decoupling sequence was optimized is indicated by a dashed rectangle.

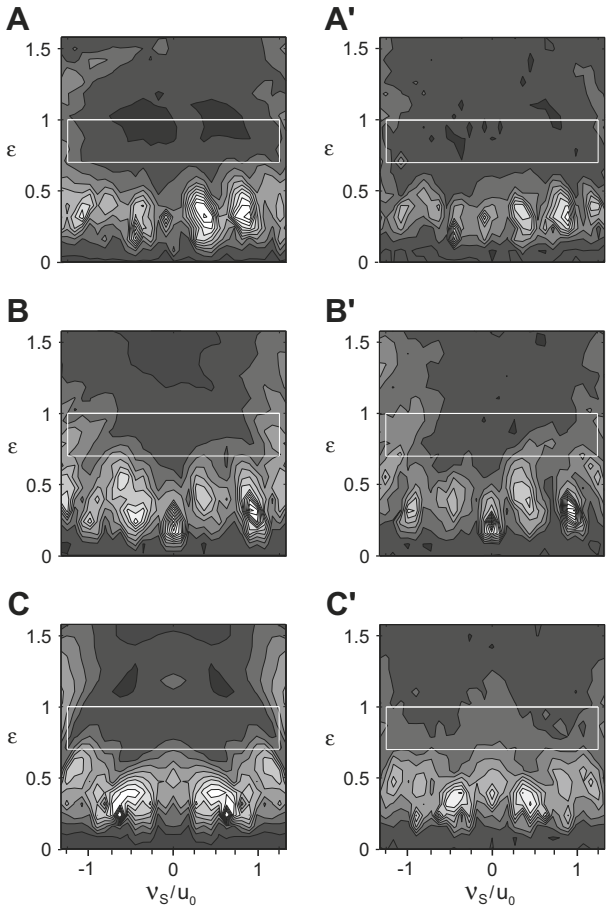

Fig. 6. Maximum sideband amplitudes (normalized relative to the perfectly decoupled peak amplitude) in simulated (left column) and experimental (right column) spectra are shown as a function of relative offset ν_S/u_0 and rf scaling ϵ for (A) TRACK-1, (B) MLEV-16 and (C) WALTZ-16. The same contour levels were used as in Fig. 5, the range $-1.25 \leqslant \nu_S/u_0 \leqslant 1.25$ and $0.7 \leqslant \epsilon \leqslant 1$ for which the TRACK-1 decoupling sequence was optimized is indicated by a white rectangle.

tional iterative schemes of pulse sequence construction and it is interesting to compare the tracking-based optimization of decoupling sequences with optimizations based on a desirable effective Hamiltonian. The effective (or average) Hamiltonian approach [23,55] allows one to optimize decoupling sequences based on a relatively small number of pulse sequence parameters corresponding to a cyclic basis sequence. However, in practice the actual effective Hamiltonian created by a given basis sequence of finite duration can only approximate the desired effective Hamiltonian. The effects of the remaining error terms accumulate coherently for periodically repeated basis sequences. Without the availability of an efficient tracking algorithm, this problem has previously triggered the development of schemes, where deterministic decoupling sequences are embedded in stochastic ones, in order to achieve efficient decoupling on short and long time scales [59–61]. Also, depending on the kind of remaining error terms in the effective Hamiltonian, their effect can be more or less detrimental, and in spectroscopic applications it is therefore preferable to directly optimize for the desired evolution of the density operator, rather than trying to approach a desired effective Hamiltonian. Still, it is instructive to use concepts from average Hamiltonian theory [23] to analyze aspects of tracking-based decoupling in the Supplementary material, the detailed time-dependence of the toggling frame defined by the TRACK-1 sequence is shown, demonstrating that TRACK-1 consists of a series of inversion elements that average the toggling frame coupling term to zero.

The TRACK-1 sequence was optimized for typical system parameters of *in vivo* applications, in order to demonstrate the presented spin-tracking approach. Although the TRACK-1 sequence was specifically optimized for a dwell time ΔT of 1 ms, the sequence also works well for shorter dwell times (and correspondingly larger spectral widths), as discussed in the previous section. The optimization criteria can easily be modified to match the experimental constraints of any given application, such as the offset range or the experimentally determined distribution of rf scalings. It is expected that the tracking approach can also be applied to broadband decoupling in situations with less restricted rf power constraints, such as in protein spectroscopy at high magnetic fields. In the present study, the rf power of the decoupling sequence was limited by limiting the maximum rf amplitude u_{max}, resulting in decoupling sequences with constant rf amplitude that are easy to implement and do not require linear amplifiers. Even better decoupling performance may be possible by only limiting the rf power (rather than the rf amplitude) as described in the original GRAPE paper [29] and as applied for rf power limited excitation and inversion pulses [38].

The TRACK-1 sequence creates significantly smaller decoupling sidebands compared to conventional decoupling sequences (c.f. Fig. 6) although the suppression of decoupling sidebands was not

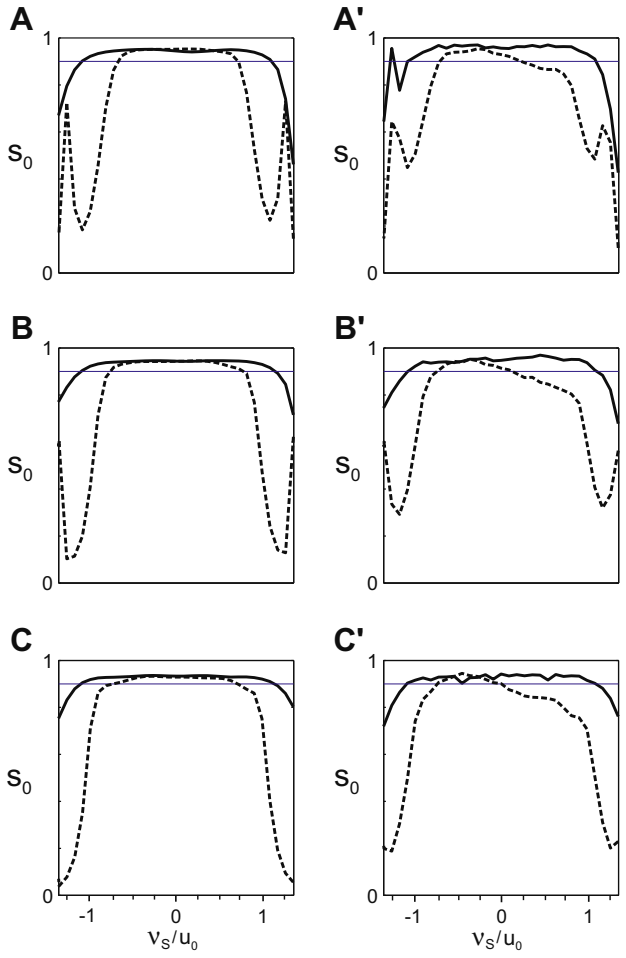

Fig. 7. For rf scaling factors $\epsilon = 0.87$ (top), $\epsilon = 0.79$ (middle), and $\epsilon = 0.71$ (bottom panel), cross sections of the plots of Fig. 5 are shown, representing simulated (left column) and experimental (right column) signal amplitudes S_0 (normalized relative to the perfectly decoupled peak amplitude) as a function of relative offset ν_S/u_0 for TRACK-1 (solid curve) and MLEV-16 (dashed curve). The horizontal line indicates a normalized signal amplitude of 0.9, corresponding to the threshold used in [19] to define the decoupling bandwidth.

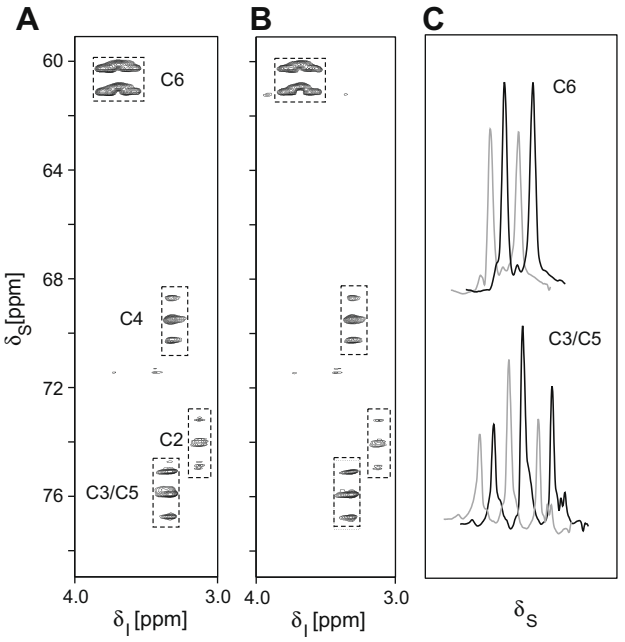

Fig. 8. Experimental two-dimensional HSQC spectra with (A) TRACK-1 and (B) MLEV-16 ^{13}C decoupling during the detection period t_2 of α/β-D-glucose dissolved in D_2O at a ^1H frequency of 200 MHz are shown. In both experiments, a constant nominal rf amplitude for decoupling of $u_0 = 400$ Hz was used and the transmitter frequency was set at 69 ppm. (C) Shows cross sections (solid spectra: TRACK-1 decoupling, gray spectra: MLEV-16 decoupling) of two groups of cross peaks corresponding to C_6 and C_3/C_5 for the two glucose anomers.

explicitly included as an optimization criterion in the definition of the overall quality factor Φ, which simply reflects the average amplitude of the decoupled signals. If decoupling sidebands need to be further reduced, this may be achieved by introducing a penalty on modulations in the FID or by other approaches based on multiple scans. The TRACK-1 sequence was optimized for a specific heteronuclear J coupling constant of 140 Hz. However, simulations show that the decoupling quality is relatively insensitive to a variation of the coupling constant, although the decoupling quality slightly increases with decreasing J and decreases with increasing J, as expected. If necessary, increased robustness with respect to variations of J coupling constants in a given range can be explicitly taken into account in the optimization by a straight-forward generalization of the overall quality factor Φ, c.f. Eq. (14). In applications where only relatively small long-range coupling constants are expected, decoupling sequences should be specifically optimized for these coupling constants. Similarly, robustness with respect to variations of relaxation times could be explicitly included as an optimization criterion if necessary. In the demonstration example considered here, the operators I_x, $2I_yS_x$, $2I_yS_y$, $2I_yS_z$ were assumed to have identical relaxation rates, reflecting T_2 (or T_2^*). In many situations, this is a reasonable approximation, but as pointed out above, a full relaxation matrix treatment can be applied if this approximation is not valid (c.f. Appendix 1).

Although it is possible to extend the presented tracking-based approach to more complicated spin systems, here we focused on the simple case of an isolated pair of two heteronuclear spins 1/2, labeled I and S (corresponding e.g. to ^1H and ^{13}C), where the decoupling sequence is applied to spin S. This setting also applies to ^{13}C decoupling of methylene (CH_2) and methyl (CH_3) groups, corresponding to I_2S and I_3S spin systems. In this case, each spin I is coupled only to a single spin S and additional $S - I'$ couplings commute with the Hamiltonian of Eq. (6). The same is true for additional homonuclear $I - I'$ couplings in the weak coupling limit [65,66]. In addition to heteronuclear decoupling in liquid-state NMR, the tracking-based pulse sequences are expected to find further applications in spectroscopy and quantum information processing [59–64], such as heteronuclear decoupling in solid-state NMR in the presence of magic angle sample spinning and homonuclear decoupling.

Acknowledgments

J.L.N. acknowledges support from the DAAD, N.K. acknowledges support from NSF 0724057 and S.J.G. acknowledges support from the DFG (GI 203/6-1), European integrated programs Bio-DNP and QAP, SFB 631, and the Fonds der Chemischen Industrie. Experiments were performed at the Bavarian NMR center at TU München and we thank Dr. Raimund Marx and Dr. Wolfgang Eisenreich for their help in simulations and experiments.

Appendix 1. Gradient for the optimization of decoupling sequences using a full relaxation matrix approach

In general, the evolution of the density operator $\rho(t_m)$ after the mth time slice of the decoupling sequence (c.f. Fig. 1) can be calcu-

lated using a full relaxation matrix treatment and the resulting gradient for the optimization of decoupling sequences is summarized here. For an arbitrary initial density operator $\rho(t_0)$ corresponding to the superket $\hat{\rho}(t_0)$ [55], the density operator (in superket form) at time t_m is given by

$$\hat{\rho}(t_m) = \hat{L}_m \dots \hat{L}_1 \ \hat{\rho}(t_0), \tag{23}$$

with

$$\hat{L}_n = \exp\left\{\left(-\mathrm{i}\ \hat{\mathscr{H}}'_n + \hat{\Gamma}\right)\ \Delta t\right\}, \tag{24}$$

where $-\mathrm{i}\ \hat{\mathscr{H}}'_n + \hat{\Gamma}$ is the Liouville superoperator, $\hat{\mathscr{H}}'_n$ is the Hamilton superoperator during the nth time slice and $\hat{\Gamma}$ is the relaxation superoperator. Hence, the signal amplitude s_k at time point $T_k = k\Delta T = kM\Delta t = t_{kM}$ can be expressed as

$$\begin{aligned} s_k &= \langle \hat{C}(T_k) \mid \hat{L}_{kM} \dots \hat{L}_1 \ \hat{\rho}(t_0)\rangle \\ &= \left\langle \underbrace{\hat{L}^\dagger_{j+1} \dots \hat{L}^\dagger_{kM}\ \hat{C}(T_k)}_{\hat{\lambda}_k(t_j)} \middle| \underbrace{\hat{L}_j \dots \hat{L}_1\ \hat{\rho}(t_0)}_{\hat{\rho}(t_j)} \right\rangle, \end{aligned} \tag{25}$$

with $\hat{C}(T_k) = \hat{I}_x$ and $t_0 \leqslant t_j \leqslant t_{kM} = T_k$.

In complete analogy to the derivation in [29], to first order in Δt we find

$$\frac{\delta s_k}{\delta u_\alpha(j)} = -\mathrm{i}\ 2\pi\epsilon\Delta t\ \langle \lambda_k(t_j) \mid [S_\alpha, \rho(t_j)]\rangle, \tag{26}$$

where $\alpha = x$ or y. According to Eq. (13), the quality factor for decoupling representing the signal amplitude of a decoupled resonance line for a rf scaling ϵ and offset ν_S is given by

$$\phi(\epsilon, \nu_S) = \frac{1}{N+1}\sum_{k=0}^{N} s_k. \tag{27}$$

Now we are interested to calculate the effect on the quality factor $\phi(\epsilon, \nu_S)$ if the control amplitudes $u_x(j)$ or $u_y(j)$ are varied in the jth time slice, i.e. between the time points t_{j-1} and t_j. This time slice is located between the detection points T_l and T_{l+1}, where $l = \lfloor j/M \rfloor$ is the truncated value (also called floor function or integral value) of the ratio j/M, i.e. the number of complete intervals ΔT between the time points t_0 and t_j. Note that the controls $u_x(j)$ or $u_y(j)$ only have an effect on the detected signal s_k for $k > l = \lfloor j/M \rfloor$.

Hence, to first order in Δt, we find

$$\begin{aligned} \frac{\delta\phi(\epsilon, \nu_S)}{\delta u_\alpha(j)} &= \frac{1}{N+1}\sum_{k=1}^{N}\frac{\delta s_k}{\delta u_\alpha(j)} = \frac{1}{N+1}\sum_{k>l}\frac{\delta s_k}{\delta u_\alpha(j)} \\ &= \mathrm{i}\ 2\pi\epsilon\Delta t\ \frac{1}{N+1}\sum_{k>l}\ \langle \lambda_k(t_j) \mid [S_\alpha, \rho(t_j)]\rangle \\ &= \mathrm{i}\ 2\pi\epsilon\Delta t\ \frac{1}{N+1}\sum_{k>l}\ \langle S_\alpha \mid [\rho(t_j), \lambda_k(t_j)]\rangle, \end{aligned} \tag{28}$$

where in the last line we used the fact that the operators S_x and S_y are Hermitian and also that the costate operators $\lambda_k(t_j)$ are Hermitian for Hermitian target operators $C(T_k)$.

Appendix 2. Gradient for the optimization of decoupling for a simple relaxation model

If all elements of the density operator have the same relaxation rate κ, the density operator at time t_m is simply given by

$$\rho(t_m) = \exp\{-\kappa\ t_m\}\ \rho'(t_m), \tag{29}$$

where

$$\rho'(t_m) = U_m \dots U_1\ \rho(t_0)\ U_1^\dagger \dots U_m^\dagger, \tag{30}$$

is the density operator at time t_m in the absence of relaxation. The propagator U_n for the nth time slice is given by

$$U_n = \exp\{-\mathrm{i}\ \Delta t\ \mathscr{H}'_n\}, \tag{31}$$

where

$$\mathscr{H}'_n = \mathscr{H}^S_{off} + \mathscr{H}^{IS}_J + 2\pi\ \epsilon\ (u_x(n)S_x + u_y(n)S_y), \tag{32}$$

and $u_x(n)$ and $u_y(n)$ are the constant control amplitudes during this time slice. The signal amplitude s_k for time point $T_k = k\Delta T = kM\Delta t = t_{kM}$ is given by

$$\begin{aligned} s_k &= \exp\{-\kappa T_k\}\,\langle C(T_k) \mid U_{kM} \dots U_1\,\rho(t_0)\,U_1^\dagger \dots U_{kM}^\dagger\rangle \\ &= \exp\{-\kappa T_k\}\left\langle \underbrace{U^\dagger_{j+1} \dots U^\dagger_{kM}\,C(T_k)\,U_{kM} \dots U_{j+1}}_{\lambda'_k(t_j)} \middle| \underbrace{U_j \dots U_1\,\rho(t_0)\,U_1^\dagger \dots U_j^\dagger}_{\rho'(t_j)} \right\rangle, \end{aligned} \tag{33}$$

where $C(T_k) = I_x$ and $t_0 \leqslant t_j \leqslant t_{kM} = T_k$.

In this case, to first order in Δt the gradient $\delta s_k/\delta u_\alpha(j)$ is given by

$$\frac{\delta s_k}{\delta u_\alpha(j)} = -\mathrm{i}\ 2\pi\epsilon\Delta t\ \exp\{-\kappa\ T_k\}\ \langle \lambda'_k(t_j) \big| [S_\alpha, \rho'(t_j)]\rangle, \tag{34}$$

where $\alpha = x$ or y. Now we want to calculate the effect on the quality factor $\phi(\epsilon, \nu_S)$, c.f. Eqs. (13) and (31) if the control amplitude $u_x(j)$ or $u_y(j)$ are varied in the jth time slice, i.e. between the time points t_{j-1} and t_j. This time slice is located between the detection points T_l and T_{l+1}, where $l = \lfloor j/M \rfloor$ is the truncated value of the ratio j/M, i.e. the number of complete intervals ΔT between the time points t_0 and t_j. In analogy to the derivation in Appendix 1, to first order in Δt, we find

$$\begin{aligned} \frac{\delta\phi(\epsilon, \nu_S)}{\delta u_\alpha(j)} &= \frac{1}{N+1}\sum_{k>l}\frac{\delta s_k}{\delta u_\alpha(j)} \\ &= \mathrm{i}\ 2\pi\epsilon\Delta t\ \frac{1}{N+1} \\ &\quad \times \sum_{k>l}\ \exp\{-\kappa\ T_k\}\ \langle \lambda'_k(t_j) \big| [S_\alpha, \rho'(t_j)]\rangle \\ &= \mathrm{i}\ 2\pi\epsilon\Delta t\ \frac{1}{N+1} \\ &\quad \times \sum_{k>l}\ \exp\{-\kappa\ T_k\}\ \langle S_\alpha \big| [\rho'(t_j), \lambda'_k(t_j)]\rangle. \end{aligned} \tag{35}$$

Appendix 3. Efficient calculation of (t_j)

The definition (c.f. Eq. (18)) of

$$\Lambda(t_j) = \sum_{k>l}\ \exp\{-\kappa\ T_k\}\ \lambda'_k(t_j), \tag{36}$$

appears to imply that it is necessary to calculate N unitary backward evolutions of the costate operators $\lambda_k(t_j)$ between the time points T_k and t_0 in order to calculate $\Lambda(t_j)$ for all time points $t_0 \leqslant t_j \leqslant T_N$. However, only a single unitary backward evolution is required between T_N and T_0 by taking advantage of the fact that for any unitary transformation

$$\sum_k UA_kU^\dagger = U\left(\sum_k A_k\right)U^\dagger. \tag{37}$$

Using the definition of $\lambda'_k(t_j)$ (c.f. Eq. (17)), $\Lambda(t_j)$ can be written as

$$\Lambda(t_j) = \sum_{k>l}\ \exp\{-\kappa\ T_k\}\ U^\dagger_{j+1} \dots U^\dagger_{kM}\ C(T_k)\ U_{kM} \dots U_{j+1}. \tag{38}$$

Between two time points $T_i = t_{iM}$ and $T_{i-1} = t_{(i-1)M}$, the index j of the time slices runs from $\{iM\}$ to $\{(i-1)M+1\}$ and $l = \lfloor j/M \rfloor = (i-1)$ is constant. The condition $k > l = (i-1)$ in the sum of Eq. (38) implies that we only need to calculate the backward evolution of the operators $\lambda_i(t_j), \ldots \lambda_N(t_j)$ and for each time slice Δt the unitary transformations are identical. As a result, for a given $\Lambda(t_j)$ we can calculate $\Lambda(t_{j-1}) = \Lambda(t_j - \Delta t)$ by

$$\Lambda(t_j - 1) = \begin{cases} U_j^\dagger \Lambda(t_j) U_j \\ \quad \text{if} \quad \lfloor j/M \rfloor = \lfloor (j-1)/M \rfloor \\ U_j^\dagger \Lambda(t_j) U_j + C_{\lfloor j/M \rfloor} \exp\{-\kappa\ T_{\lfloor j/M \rfloor}\} \\ \quad \text{if} \quad \lfloor j/M \rfloor > \lfloor (j-1)/M \rfloor \end{cases}. \tag{39}$$

where $C_{\lfloor j/M \rfloor} = \lambda'_{\lfloor j/M \rfloor}(T_{\lfloor j/M \rfloor})$, which in the case of decoupling is identical to I_x. With

$$\Lambda(T_N) = \lambda_N \exp\{-\kappa\ T_N\}, \tag{40}$$

as a starting point, the operator $\Lambda(t_j)$ can iteratively be calculated using Eq. (39) for all time points t_j between $T_N = t_{NM}$ and T_0.

Appendix 4. Reduced Liouville space for decoupling simulation and optimization

As discussed in the theory section, $\mathscr{H}^I_{off}$ commutes with the terms $\mathscr{H}^S_{off}$, $\mathscr{H}^{IS}_J$, and $\mathscr{H}^S_{rf}(t)$. Hence the offset effect of spin I can be separated and without loss of generality, it is sufficient to consider the simplified Hamiltonian

$$\mathscr{H}'(t) = \mathscr{H}^S_{off} + \mathscr{H}^{IS}_J + \mathscr{H}^S_{rf}(t), \tag{41}$$

for the simulation and optimization of heteronuclear decoupling sequences, i.e. spin I can be assumed to be on resonance. Also without loss of generality, we assume the initial density operator to be

$$\rho(0) = I_x. \tag{42}$$

In the absence of relaxation effects, the initial density operator $\rho(0) = I_x$ can only evolve to the operators $2I_yS_x$, $2I_yS_y$, $2I_yS_z$ under the action of $\mathscr{H}'(t)$, i.e. the dynamics are restricted to the four-dimensional subspace of the complete 15-dimensional Liouville space [56–58]. Even in the presence of relaxation, the dynamics are limited to this subspace if cross-relaxation to other operators can be neglected. In analogy to the three-dimensional Bloch vector representation of the density operator for a single uncoupled spin, the vector components of which are proportional to the expectation values of I_x, I_y, and I_z, we can combine the expectation values of the terms $2I_yS_x$, $2I_yS_y$, $2I_yS_z$, and I_x to form the elements of a real, four-dimensional reduced state vector $\vec{\rho}$ that represents the relevant terms of the density operator for the simulation and optimization of heteronuclear decoupling sequences:

$$\vec{\rho} = \begin{pmatrix} \rho_x \\ \rho_y \\ \rho_z \\ \rho_e \end{pmatrix} = \begin{pmatrix} \mathrm{Tr}\{\rho\ 2I_yS_x\} \\ \mathrm{Tr}\{\rho\ 2I_yS_y\} \\ \mathrm{Tr}\{\rho\ 2I_yS_z\} \\ \mathrm{Tr}\{\rho\ I_x\} \end{pmatrix}, \tag{43}$$

and the initial reduced state vector corresponding to the density operator $\rho(t_0) = I_x$ is given by $\vec{\rho}(t_0) = (0001)^T$.

For the simple relaxation model considered in the main text and in Appendix 2, the terms $2I_yS_x$, $2I_yS_y$ (corresponding to mixtures of zero and double quantum coherence), $2I_yS_z$ (anti-phase coherence of spin I), and I_x (in-phase coherence of spin I) are assumed to have similar relaxation rates, which can be approximated by a uniform relaxation rate κ. In this case, the reduced state vector at a time point t_m is simply given by

$$\vec{\rho}(t_m) = \exp\{-\kappa\ t_m\}\ \vec{\rho}'(t_m), \tag{44}$$

where

$$\vec{\rho}'(t_m) = \mathbf{U}_m \ldots \mathbf{U}_1\ \vec{\rho}(t_0), \tag{45}$$

is the corresponding four-dimensional reduced state vector at time t_m in the absence of relaxation. The matrix elements of the generalized rotation matrices $\mathbf{U}_n$ corresponding to the propagator for the nth time slice are explicitly given in Supplementary material (see also [56–58] for an equivalent representation of the propagators).

We also define the reduced costate vectors $\vec{\lambda}_k$ as

$$\vec{\lambda}_k = \begin{pmatrix} \lambda_{kx} \\ \lambda_{ky} \\ \lambda_{kz} \\ \lambda_{ke} \end{pmatrix} = \begin{pmatrix} \mathrm{Tr}\{\lambda_k\ 2I_yS_x\} \\ \mathrm{Tr}\{\lambda_k\ 2I_yS_y\} \\ \mathrm{Tr}\{\lambda_k\ 2I_yS_z\} \\ \mathrm{Tr}\{\lambda_k\ I_x\} \end{pmatrix}, \tag{46}$$

and the vectors $\vec{\lambda}_k(T_k)$ corresponding to the costates $\lambda_k(T_k) = C(T_k) = I_x$ are given by $\vec{\lambda}_k(T_k) = (0001)^T$. In the absence of relaxation, the reduced state vector $\vec{\lambda}'_k(t_m)$ at time point $t_m \leqslant t_k$ is given by

$$\vec{\lambda}'_k(t_m) = \mathbf{U}^T_{m+1} \ldots \mathbf{U}^T_k\ \vec{\lambda}_k(T_k), \tag{47}$$

where $\mathbf{U}^T_n = \mathbf{U}^{-1}_n$ is the transpose of $\mathbf{U}_n$.

With the reduced state vector $\vec{\rho}'$ and the costate vectors $\vec{\lambda}'_k$ at each time point t_j, to first order in Δt the derivatives $\delta s_k/\delta u_\alpha(j)$ can be calculated in a straight-forward way based on Eq. (34):

$$\frac{\delta s_k}{\delta u_x(j)} = 2\pi\epsilon\Delta t\ \exp\{-\kappa\ T_k\}\ \left(\rho'_y(t_j)\lambda'_{kz}(t_j) - \rho'_z(t_j)\lambda'_{ky(t_j)}\right), \tag{48}$$

and

$$\frac{\delta s_k}{\delta u_y(j)} = 2\pi\epsilon\Delta t\ \exp\{-\kappa\ T_k\}\ \left(\rho'_z(t_j)\lambda'_{kx}(t_j) - \rho'_x(t_j)\lambda'_{kz}(t_j)\right). \tag{49}$$

Based on Eqs. (15), (48), and (49), the gradient $\delta\phi(\epsilon, v_S)/\delta u_\alpha(j)$ for $0 \leqslant j \leqslant MN$ and $\alpha = x$ or y is given by

$$\frac{\delta\phi(\epsilon, v_S)}{\delta u_x(j)} = 2\pi\epsilon\Delta t\ \frac{1}{N+1}\ \left(\rho'_y(t_j)\Lambda_z(t_j) - \rho'_z(t_j)\Lambda_y(t_j)\right), \tag{50}$$

and

$$\frac{\delta\phi(\epsilon, v_S)}{\delta u_y(j)} = 2\pi\epsilon\Delta t\ \frac{1}{N+1}\ \left(\rho'_z(t_j)\Lambda_x(t_j) - \rho'_x(t_j)\Lambda_z(t_j)\right). \tag{51}$$

The required vectors $\vec{\rho}'(t_j)$ and $\vec{\Lambda}(t_j)$ can be obtained by one forward evolution of the reduced state vector $\vec{\rho}'(t_j)$ (see Eq. (45)) and by one backward evolution of the vector $\vec{\Lambda}(t_j)$, starting from $\vec{\Lambda}(T_N) = \exp\{-\kappa\ T_N\}\vec{\lambda}(T_N) = \exp\{-\kappa\ T_N\}\vec{C}_N = \exp\{-\kappa\ T_N\}(0,0,0,1)^T$. In analogy to Appendix 3, for each time slice Δt, the backward evolution of $\vec{\Lambda}(t_n)$ can efficiently be calculated by

$$\vec{\Lambda}(t_n - 1) = \begin{cases} \mathbf{U}^T_j\ \vec{\Lambda}(t_n) \\ \quad \text{if} \quad \lfloor n/M \rfloor = \lfloor (n-1)/M \rfloor \\ \mathbf{U}^T_n\ \vec{\Lambda}(t_n) + \vec{C}_{\lfloor n/M \rfloor} \exp\{-\kappa\ T_{\lfloor n/M \rfloor}\} \\ \quad \text{if} \quad \lfloor n/M \rfloor > \lfloor (n-1)/M \rfloor \end{cases}, \tag{52}$$

where $\vec{C}_{\lfloor n/M \rfloor} = \vec{\lambda}_{\lfloor n/M \rfloor}(T_{\lfloor n/M \rfloor})$, which in the case of decoupling is identical to $(0,0,0,1)^T$.

Appendix E. Supplementary data

Supplementary data associated with this article can be found, in the online version, at doi:10.1016/j.jmr.2009.07.024.

References

[1] M.H. Levitt, R. Freeman, T.A. Frenkiel, Broadband decoupling in high-resolution NMR spectroscopy, Adv. Magn. Reson. 11 (1983) 47–110.
[2] A.J. Shaka, J. Keeler, Broadband spin decoupling in isotropic liquids, Prog. NMR Spectrosc. 19 (1987) 47–129.

[3] W.A. Anderson, R. Freeman, Influence of a second radiofrequency field on high-resolution nuclear magnetic resonance spectra, J. Chem. Phys. 37 (1962) 85–103.
[4] R.R. Ernst, Nuclear magnetic double resonance with an incoherent radio-frequency field, J. Chem. Phys. 45 (1966) 3845–3861.
[5] M.H. Levitt, R. Freeman, T. Frenkiel, Broadband heteronuclear decoupling, J. Magn. Reson. 47 (1982) 328–330.
[6] J.S. Waugh, Theory of broadband spin decoupling, J. Magn. Reson. 50 (1982) 30–49.
[7] A.J. Shaka, J. Keeler, T. Frenkiel, R. Freeman, An improved sequence for broadband decoupling: WALTZ-16, J. Magn. Reson. 52 (1983) 335–338.
[8] A.J. Shaka, P.B. Barker, R. Freeman, Computer-optimized decoupling scheme for wideband applications and low-level operation, J. Magn. Reson. 64 (1985) 547–552.
[9] T. Fujiwara, K. Nagayama, Composite inversion pulses with frequency switching and their application to broadband decoupling, J. Magn. Reson. 77 (1988) 53–63.
[10] E.R.P. Zuiderweg, S.W. Fesik, Band-selective heteronuclear decoupling using shaped pulses as an aid in measuring long-range heteronuclear coupling constants, J. Magn. Reson. 93 (1991) 653–658.
[11] U. Eggenberger, P. Schmidt, M. Sattler, S.J. Glaser, C. Griesinger, Frequency-selective decoupling with recursively expanded soft pulses in multinuclear NMR, J. Magn. Reson. 100 (1992) 604–610.
[12] M.A. McCoy, L. Mueller, Selective decoupling, J. Magn. Reson. A 101 (1993) 122–130.
[13] Z. Starcuk Jr., K. Bartusek, Z. Starcuk, Heteronuclear broadband spin-flip decoupling with adiabatic pulses, J. Magn. Reson. A 107 (1994) 24–31.
[14] M.R. Bendall, Broadband and narrowband spin decoupling using adiabatic spin flips, J. Magn. Reson. A 112 (1995) 26–129.
[15] T.E. Skinner, M.R. Bendall, Peak power and efficiency in hyperbolic secant decoupling, J. Magn. Reson. A 123 (1995) 111–115.
[16] E. Kupce, R. Freeman, Optimized adiabatic pulses for wideband spin inversion, J. Magn. Reson. A 118 (1996) 299–303.
[17] R. Fu, G. Bodenhausen, Evaluation of adiabatic frequency-modulated schemes for broadband decoupling in isotropic liquids, J. Magn. Reson. A 119 (1996) 129–133.
[18] H. Geen, Theoretical design of amplitude-modulated pulses for spin decoupling in nuclear magnetic resonance, J. Phys. B 29 (1996) 1699–1710.
[19] R.A. de Graaf, Theoretical and experimental evaluation of broadband decoupling techniques for in vivo nuclear magnetic resonance spectroscopy, Magn. Reson. Med. 53 (2005) 1297–1306.
[20] M.H. Levitt, R. Freeman, T. Frenkiel, Supercycles for broadband heteronuclear decoupling, J. Magn. Reson. 50 (1982) 157–160.
[21] R. Tycko, Iterative methods in the design of pulse sequences for NMR excitation, Adv. Magn. Reson. 15 (1990).
[22] J.J. Kotyk, J.R. Garbow, T. Gullion, Improvements in proton-detected NMR spectroscopy using spin-flip decoupling. An application to heteronuclear chemical shift correlation, J. Magn. Reson. 89 (1990) 647–653.
[23] U. Haeberlen, High resolution NMR in solids: selective averaging, Adv. Magn. Reson. Suppl. 1 (1976).
[24] A. Bryson Jr., Y.-C. Ho, Applied Optimal Control, Hemisphere, Washington, DC, 1975.
[25] T.O. Reiss, N. Khaneja, S.J. Glaser, Time-optimal coherence-order-selective transfer of in-phase coherence in heteronuclear IS spin systems, J. Magn. Reson. 154 (2002) 192–195.
[26] N. Khaneja, F. Kramer, S.J. Glaser, Optimal experiments for maximizing coherence transfer between coupled spins, J. Magn. Reson. 173 (2005) 116–124.
[27] D. Stefanatos, N. Khaneja, S.J. Glaser, Optimal control of coupled spins in presence of longitudinal relaxation, Phys. Rev. A 69 (2004) 022319.
[28] D.P. Früh, T. Ito, J.S. Li, G. Wagner, S.J. Glaser, N. Khaneja, Sensitivity enhancement in NMR of macromolecules by application of optimal control theory, J. Biomol. NMR 32 (2005) 23–30.
[29] N. Khaneja, T. Reiss, C. Kehlet, T. Schulte-Herbrüggen, S.J. Glaser, Optimal control of coupled spin dynamics: design of NMR pulse sequences by gradient ascent algorithms, J. Magn. Reson. 172 (2005) 296–305.
[30] Z. Tošner, T. Vosegaard, C. Kehlet, N. Khaneja, S.J. Glaser, N.C. Nielsen, Optimal control in NMR spectroscopy: numerical implementation in SIMPSON, J. Magn. Reson. 197 (2009) 120–134.
[31] T.E. Skinner, T.O. Reiss, B. Luy, N. Khaneja, S.J. Glaser, Reducing the duration of broadband excitation pulses using optimal control with limited rf amplitude, J. Magn. Reson. 167 (2004) 68–74.
[32] T.E. Skinner, T.O. Reiss, B. Luy, N. Khaneja, S.J. Glaser, Tailoring the optimal control cost function to a desired output: application to minimizing phase errors in short broadband excitation pulses, J. Magn. Reson. 172 (2005) 7–23.
[33] K. Kobzar, T.E. Skinner, N. Khaneja, S.J. Glaser, B. Luy, Exploring the limits of broadband excitation and inversion pulses, J. Magn. Reson. 170 (2004) 236–243.
[34] K. Kobzar, B. Luy, N. Khaneja, S.J. Glaser, Pattern pulses: design of arbitrary excitation profiles as a function of pulse amplitude and offset, J. Magn. Reson. 173 (2005) 229–235.
[35] T.E. Skinner, K. Kobzar, B. Luy, R. Bendall, W. Bermel, N. Khaneja, S.J. Glaser, Optimal control design of constant amplitude phase-modulated pulses: application to calibration-free broadband excitation, J. Magn. Reson. 179 (2006) 241–249.
[36] J.L. Neves, B. Heitmann, T.O. Reiss, H.H.R. Schor, N. Khaneja, S.J. Glaser, Exploring the limits of polarization transfer efficiency in homonuclear three spin systems, J. Magn. Reson. 181 (2006) 126–134.
[37] N.I. Gershenzon, K. Kobzar, B. Luy, S.J. Glaser, T.E. Skinner, Optimal control design of excitation pulses that accommodate relaxation, J. Magn. Reson. 188 (2007) 330–336.
[38] K. Kobzar, T.E. Skinner, N. Khaneja, S.J. Glaser, B. Luy, Exploring the limits of excitation and inversion pulses II. RF-power optimized pulses, J. Magn. Reson. 194 (2008) 58–66.
[39] Z. Tošner, S.J. Glaser, N. Khaneja, N.C. Nielsen, Effective Hamiltonians by optimal control: solid-state NMR double-quantum planar and isotropic dipolar recoupling, J. Chem. Phys. 125 (2006) 1–10.
[40] T. Schulte-Herbrüggen, A. Spörl, N. Khaneja, S.J. Glaser, Optimal control-based efficient synthesis of building blocks of quantum algorithms seen in perspective from network complexity towards time complexity, Phys. Rev. A 72 (2005) 1–7.
[41] R. Fisher, H. Yuan, A. Spörl, S. Glaser, Time-optimal generation of cluster states, Phys. Rev. A 79 (2009) 042304.
[42] R.W. Brockett, Finite Dimensional Linear Systems, John Wiley & Sons, New York, 1970.
[43] R.M. Hirschorn, J.H. Davis, Global output tracking for nonlinear systems, SIAM J. Control Optim. 26 (1988) 1321–1330.
[44] P. Gross, H. Singh, H. Rabitz, K. Mease, G.H. Huang, Inverse quantum-mechanical control: a means for design and a test of intuition, Phys. Rev. A 47 (1993) 4593–4604.
[45] M. Sugawara, General formulation of locally designed control theory for quantum system, J. Chem. Phys. 118 (2003) 6784–6800.
[46] W. Zhu, H. Rabitz, Quantum control design via adaptive tracking, J. Chem. Phys. 119 (2003) 3619–3625.
[47] M. Wenin, W. Pötz, Optimal control of a single qubit by direct inversion, Phys. Rev. A 74 (2006) 022319.
[48] R.W. Brockett, Characteristic phenomena and model problems in nonlinear control, in: Proc. of the 1996 IFAC Congress, vol. G, 1996, pp. 135–140.
[49] K. Morgansen, R.W. Brockett, Nonholonomic control based on approximate inversion, in: Proc. of the 1999 American Control Conference, San Diego, CA, 1999, pp. 3515–3519.
[50] Y. Ohtsuki, G. Turinici, H. Rabitz, Generalized monotonically convergent algorithm for solving quantum optimal control problems, J. Chem. Phys. 120 (2004) 5509–5517.
[51] I. Serban, J. Werschnik, E.K.U. Gross, Optimal control of time-dependent targets, Phys. Rev. A 71 (2005) 053810.
[52] J. Werschnik, E.K.U. Gross, Quantum optimal control theory, J. Phys. B At. Mol. Opt. Phys. 40 (2005) R175–R211.
[53] H. Jirari, W. Pötz, Quantum optimal control theory and dynamical coupling in the spin-boson model, Phys. Rev. A 74 (2006) 022306.
[54] J.P. Palao, R. Kosloff, C.P. Koch, Protecting coherence in optimal control theory: state-dependent constraint approach, Phys. Rev. A 77 (2008) 063412.
[55] R.R. Ernst, G. Bodenhausen, A. Wokaun, Principles of Nuclear Magnetic Resonance in One and Two Dimensions, Clarendon Press, Oxford, 1987.
[56] T.E. Skinner, M.R. Bendall, Exact product operator evolution of weakly coupled spin-1/2 I_mS_n systems during arbitrary rf irradiation of the I spins, J. Magn. Reson. 141 (1999) 271–285.
[57] M.R. Bendall, T.E. Skinner, Comparison and use of vector and quantum descriptions of *J* coupled spin evolution during RF irradiation of one spin in an IS spin system, J. Magn. Reson. 143 (2000) 329–351.
[58] T.E. Skinner, M.R. Bendall, *J*-coupling and chemical-shift evolution during I-spin irradiation of I_mS_n systems: product operator solutions and applications, Conc. Magn. Reson. 14 (2002) 287–307.
[59] L.F. Santos, L. Viola, Advantages of randomization in coherent quantum dynamical control, New J. Phys. 10 (2008) 083009.
[60] O. Kern, G. Alber, Controlling quantum systems by embedded dynamical decoupling schemes, Phys. Rev. Lett. 95 (2005) 250501.
[61] L.F. Santos, L. Viola, Enhanced convergence and robust performance of randomized dynamical decoupling, Phys. Rev. Lett. 97 (2006) 150501.
[62] L. Viola, S. Lloyd, Dynamical suppression of decoherence in two-state quantum systems, Phys. Rev. A 58 (1998) 2733–2744.
[63] K. Khodjasteh, D.A. Lidar, Fault-tolerant quantum dynamical decoupling, Phys. Rev. Lett. 95 (2005) 180501.
[64] D. Rossini, P. Facchi, R. Fazio, G. Florio, D.A. Lidar, S. Pascazio, F. Plastina, P. Zanardi, Bang–bang control of a qubit coupled to a quantum critical spin bath, Phys. Rev. A 77 (2008) 052112.
[65] A.J. Shaka, P.B. Barker, R. Freeman, Three-spin effects in broadband decoupling, J. Magn. Reson. 71 (1987) 520–531.
[66] D. Suter, V. Schenker, A. Pines, Theory of broadband heteronuclear decoupling in multispin systems, J. Magn. Reson. 73 (1987) 90–98.